Stability and decay rates of nonisotropic attractive Bose-Einstein condensates

C. Huepe,[1,4] L. S. Tuckerman,[2] S. Métens,[3,4] and M. E. Brachet[4]
[1]*Department of Engineering Sciences and Applied Mathematics, Northwestern University, 2145 Sheridan Road, Evanston, Illinois 60208, USA*
[2]*Laboratoire d'Informatique pour la Mécanique et les Sciences de l'Ingénieur, Boîte Postale 133, 91403 Orsay, France*
[3]*Laboratoire de Physique Théorique de la Matière Condensée, Université Paris VII, Paris, France*
[4]*Laboratoire de Physique Statistique de l'Ecole Normale Supérieure, associé au CNRS et aux Universités Paris VI et VII, 24 Rue Lhomond, 75231 Paris, France*
(Received 3 December 2002; published 27 August 2003)

Nonisotropic attractive Bose-Einstein condensates are investigated numerically with Newton and inverse Arnoldi methods. The stationary solutions of the Gross-Pitaevskii equation and their linear stability are computed. Bifurcation diagrams are calculated and used to find the condensate decay rates corresponding to macroscopic quantum tunneling, two-three-body inelastic collisions, and thermally induced collapse. Isotropic and nonisotropic condensates are compared. The effect of anisotropy on the bifurcation diagram and the decay rates is discussed. Spontaneous isotropization of the condensates is found to occur. The influence of isotropization on the decay rates is characterized near the critical point.

DOI: 10.1103/PhysRevA.68.023609 PACS number(s): 03.75.Kk, 32.80.Pj, 47.20.Ky, 05.30.Jp

I. INTRODUCTION

Experimental Bose-Einstein condensation (BEC) with attractive interactions was first realized in ultracold vapors of ^{7}Li atoms [1], opening a new field in the study of macroscopic quantum phenomena. Such attractive condensates are known to be metastable in spatially localized systems, provided that the number of condensed particles is below a critical value $\mathcal{N}_c$ [2]. Recently, Feshbach resonances in BEC of ^{85}Rb atoms were used to investigate the stability and dynamics of condensates with two-body interactions going from repulsive to attractive values [3].

Experimental atomic traps generally use a harmonic and slightly asymmetric potential. Thus, for most of the condensates produced so far, the geometry is nearly spherical. However, extremely asymmetric traps have been recently employed in experimental investigations of cigarlike [4–6] or pancakelike [7] condensates.

Various physical processes compete to determine the lifetime of attractive condensates. The processes considered in this paper are macroscopic quantum tunneling (MQT) [8,9], inelastic two- and three-body collisions (ICO) [10–12], and thermally induced collapse (TIC) [9,13]. The MQT and TIC contributions have been evaluated in the literature using a variational Gaussian approximation to the condensate wave function. However, this approximation is known to be in substantial quantitative error—e.g., as high as 17% for $\mathcal{N}_c$ [8,14,15]—when compared to the exact solution of the Gross-Pitaevskii (GP) equation.

In the nearly spherical isotropic case, both the elliptic (stable) and the hyperbolic (unstable) exact stationary solutions of the GP equation were obtained numerically by Newton's method in Ref. [15]. These solution branches were shown to meet at $\mathcal{N}_c$ through a generic Hamiltonian saddle-node (HSN) bifurcation. While the Gaussian approximation presents an analogous HSN bifurcation, the amplitudes of its associated scaling laws were found to be insubstantial ($\geqslant 14\%$) error. A method for computing the unstable branch in the isotropic case via a shooting method was outlined in Ref. [16], but generalizing this procedure to higher dimensions would be inefficient, and indeed impossible in nonrectangular domains. The decay rates for the processes of MQT, ICO, and TIC were also computed, in the spherical case, from the numerical GP solutions. They were shown to obey universal scaling laws. Experimentally, significant quantitative differences were found between the exact rates and those based on the Gaussian approximation [15].

In the extreme anisotropic cases, the variational Gaussian approximation has been computed and compared to the GP solution on the elliptic (stable) branch [17,18]. This has allowed a more reliable determination of the critical value $\mathcal{N}_c$ than can be obtained by the Gaussian approximation [17]. However, a faithful determination of the lifetimes requires the computation of the hyperbolic (unstable) branch [15], which has not yet been performed in the anisotropic case.

The main purpose of the present paper is to show that it is possible to compute the full HSN bifurcation diagram and the corresponding lifetimes in extreme anisotropic cases. We will do so by studying a cigarlike and a pancakelike condensate, and will obtain their MQT, ICO and TIC decay rates. While we have concentrated, for simplicity, on these two axisymmetric cases, the numerical methods developed in this work are capable of solving the general anisotropic problem.

The paper is organized as follows. In Sec. II, we present the model considered throughout this work. After defining our working form of the GP equation, we explain the methods that we used to obtain the stationary states and their linearized stability. Section III is devoted to the numerical determination of the bifurcation diagram and stability of the stationary states. Isotropic and nonisotropic cases are compared and the dynamics is discussed in terms of the HSN bifurcation. In Sec. IV, we define and compute the decay rates. Isotropic and nonisotropic rates are discussed and their similarity is analyzed in terms of the spontaneous isotropization of condensates. Finally, Sec. V is our conclusion. Details of our numerical methods are given in the Appendix.

II. PRESENTATION OF THE MODEL

A. Gross-Pitaevskii equation

At low enough temperatures, neglecting the thermal and quantum fluctuations, a Bose-Einstein condensate can be represented by a complex wave function $\Psi(\mathbf{x},t)$ that obeys the dynamics of the GP equation [19,20]. Specifically, we consider a condensate of $\mathcal{N}$ particles of mass m and (negative) effective scattering length $\tilde{a}$ in a confining harmonic potential $V(\tilde{\mathbf{x}})=m(\tilde{\omega}_x^2\tilde{x}^2+\tilde{\omega}_y^2\tilde{y}^2+\tilde{\omega}_z^2\tilde{z}^2)/2$, where $\tilde{\mathbf{x}}=(\tilde{x},\tilde{y},\tilde{z})$ is the position vector.

These variables can be rescaled with respect to any reference frequency $\hat{\omega}$ by using the natural quantum harmonic oscillator units of time $\tau_0=1/\hat{\omega}$ and length $L_0=\sqrt{\hbar/m\hat{\omega}}$. In terms of the nondimensional variables $t=\tilde{t}/\tau_0$, $\mathbf{x}=\tilde{\mathbf{x}}/L_0$, $a=4\pi\tilde{a}/L_0$, $\omega_x=\tilde{\omega}_x/\hat{\omega}$, $\omega_y=\tilde{\omega}_y/\hat{\omega}$, and $\omega_z=\tilde{\omega}_z/\hat{\omega}$, the condensate is described by the action

$$\mathcal{A}=\int dt\left\{\int d^3x\frac{i}{2}\left(\bar{\Psi}\frac{\partial\Psi}{\partial t}-\Psi\frac{\partial\bar{\Psi}}{\partial t}\right)-\mathcal{F}\right\}, \tag{1}$$

with

$$\mathcal{F}=\mathcal{E}-\mu\mathcal{N}, \tag{2}$$

where

$$\mathcal{N}=\int d^3x|\Psi|^2, \tag{3}$$

$$\mathcal{E}=\int d^3x\left[\frac{1}{2}|\nabla\Psi|^2+V(\mathbf{x})|\Psi|^2+\frac{a}{2}|\Psi|^4\right], \tag{4}$$

$$V(\mathbf{x})=\tfrac{1}{2}(\omega_x^2x^2+\omega_y^2y^2+\omega_z^2z^2). \tag{5}$$

The Euler-Lagrange equation corresponding to $\mathcal{A}$ is our working form of the Gross-Pitaevskii equation:

$$-i\frac{\partial\Psi}{\partial t}=-\frac{\delta\mathcal{F}}{\delta\bar{\Psi}}=\left[\frac{1}{2}\nabla^2-V(\mathbf{x})-(a|\Psi|^2-\mu)\right]\Psi. \tag{6}$$

Our goal is to numerically determine the stable and unstable stationary states of Eq. (6) and the eigenvalues of Eq. (6) linearized about these stationary states. We will carry out this calculation for various values of a cylindrical potential defined by $\omega_r\equiv\omega_x=\omega_y$ and ω_z: the isotropic case $\omega_r=\omega_z$, a cigar case $\omega_r/5=\omega_z$, and a pancake case $\omega_r=\omega_z/5$. We will then use these results to calculate the condensate decay rates and compare these decay rates to those produced by the Gaussian approximation.

B. Stationary states

Stationary states of Eq. (6) corresponding to minima of $\mathcal{E}$ at a given value of $\mathcal{N}$ can be obtained by integrating to relaxation the diffusion equation

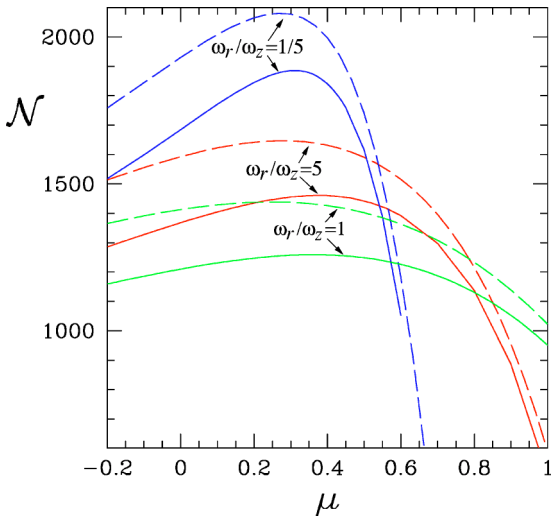

FIG. 1. Particle number $\mathcal{N}$ as a function of μ for the exact solutions (solid curves) and the Gaussian approximation (dashed curves) presented in Sec. III. From top to bottom: pancake ($\omega_r=\omega_z/5$), cigar ($\omega_r/5=\omega_z$), and isotropic ($\omega_r=\omega_z$) geometries.

$$\frac{\partial\Psi}{\partial t}=-\frac{\delta\mathcal{F}}{\delta\bar{\Psi}}=\left[\frac{1}{2}\nabla^2-V(\mathbf{x})-(a|\Psi|^2-\mu)\right]\Psi, \tag{7}$$

$$\frac{\partial\mathcal{N}}{\partial t}=0, \tag{8}$$

using initial data $\Psi(t=0)$ with a total number of particles $\mathcal{N}$. Condition (8) fixes the value of the Lagrange multiplier μ during the relaxation. This relaxation method yields both the solution Ψ and the Lagrange multiplier μ. It is equivalent to that used in Ref. [14] and can only reach the stable stationary solutions of Eq. (7). Unstable stationary solutions to Eqs. (6) and (7) are obtained by a Newton branch following method detailed in the Appendix.

Note that the Lagrange multiplier μ can only affect the solutions of Eq. (6) through a homogeneous rotating phase factor $e^{i\mu t}$, in contrast to its particle number conservation effect on Eq. (7). However, every stationary solution to Eq. (6) is indexed by the unique μ value that makes it time independent, as shown in Fig. 1.

C. Linearized stability

We now turn our attention to computing the linear stability of the GP equation about a stationary state. We first write Eq. (6) in the abbreviated form

$$-i\frac{\partial\Psi}{\partial t}=L\Psi+W(\Psi), \tag{9}$$

where

$$L\Psi\equiv\tfrac{1}{2}\nabla^2\Psi, \tag{10}$$

$$W(\Psi)\equiv[-V(\mathbf{x})-a|\Psi|^2+\mu]\Psi. \tag{11}$$

The stationary states of Eq. (9) satisfy

$$0 = L\Psi + W(\Psi). \tag{12}$$

Without loss of generality, Ψ can be chosen to be real. Our objective is to calculate the eigenpairs (λ, ψ) of the operator that results from linearizing (9) about a stationary state Ψ. [We use Ψ to designate solutions to the nonlinear problem (12) and ψ to designate eigenvectors, which are solutions to the linear problem to be defined below.] In order to correctly formulate the linear stability problem, it is necessary to first decompose $\psi = \psi^R + i\psi^I$. We write the linearized evolution equation

$$\frac{\partial \psi}{\partial t} = i[L + DW(\Psi)](\psi^R + i\psi^I), \tag{13}$$

where $DW(\Psi)$ is the Fréchet derivative, or Jacobian, of W evaluated at Ψ. $DW(\Psi)$ acts on ψ via

$$DW\psi = DW^R\psi^R + iDW^I\psi^I, \tag{14}$$

where we have omitted the functional dependence of DW, DW^R, and DW^I on Ψ, and where

$$DW^R \equiv \mu - V(\mathbf{x}) - 3a\Psi^2, \tag{15a}$$

$$DW^I \equiv \mu - V(\mathbf{x}) - a\Psi^2. \tag{15b}$$

Equation (13) is then written in matrix form as

$$\frac{\partial}{\partial t}\begin{pmatrix} \psi^R \\ \psi^I \end{pmatrix} = \begin{bmatrix} 0 & -(L + DW^I) \\ L + DW^R & 0 \end{bmatrix}\begin{pmatrix} \psi^R \\ \psi^I \end{pmatrix}. \tag{16}$$

The eigenmodes $(\lambda, \psi^R, \psi^I)$ satisfy

$$\lambda\begin{pmatrix} \psi^R \\ \psi^I \end{pmatrix} = \begin{bmatrix} 0 & -(L + DW^I) \\ L + DW^R & 0 \end{bmatrix}\begin{pmatrix} \psi^R \\ \psi^I \end{pmatrix}. \tag{17}$$

Note that this eigensystem is usually presented in the literature (see, for example, Ref. [21]) in terms of the variables

$$(\omega^{\mathrm{B}}, \psi, \psi^*) \equiv (-i\lambda, \psi^R + i\psi^I, \psi^R - i\psi^I), \tag{18}$$

as the equivalent Bogoliubov–de Gennes coupled equations

$$\omega^{\mathrm{B}}\begin{pmatrix} \psi \\ \psi^* \end{pmatrix} = \begin{bmatrix} L + DW^{\mathrm{B}} & -a\Psi^2 \\ a\Psi^2 & -(L - DW^{\mathrm{B}}) \end{bmatrix}\begin{pmatrix} \psi \\ \psi^* \end{pmatrix}, \tag{19}$$

where

$$DW^{\mathrm{B}} \equiv \mu - V(\mathbf{x}) - 2a\Psi^2. \tag{20}$$

In the following, we will work with matrix formulation (17) because it avoids a potential notational inconsistency of Eq. (19) arising from the fact that ψ and ψ^* are complex conjugates only when ω^{B} is imaginary.

It is more convenient to work with the square of the matrix in Eq. (17):

$$\lambda^2\begin{pmatrix} \psi^R \\ \psi^I \end{pmatrix} = \begin{bmatrix} -(L + DW^I)(L + DW^R) & 0 \\ 0 & -(L + DW^R)(L + DW^I) \end{bmatrix}\begin{pmatrix} \psi^R \\ \psi^I \end{pmatrix}. \tag{21}$$

Because Eq. (21) is block diagonal, it can be separated into two problems

$$\lambda^2\psi^R = -(L + DW^I)(L + DW^R)\psi^R, \tag{22a}$$

$$\lambda^2\psi^I = -(L + DW^R)(L + DW^I)\psi^I. \tag{22b}$$

Problems (22a) and (22b) are closely related. Since the operators L, DW^I, and DW^R are all self-adjoint under the standard Euclidean inner product, the operators in Eqs. (22a) and (22b) are adjoint to each other. If ψ^R is an eigenvector of Eq. (22a) with nonzero eigenvalue λ^2, then $(L + DW^R)\psi^R$ is an eigenvector of Eq. (22b) with the same eigenvalue. [Similarly, if $(\lambda, \psi^R, \psi^I)$ is an eigenmode of Eq. (17), then $(-\lambda, \psi^R, -\psi^I)$ is also an eigenmode of Eq. (17).] Thus, we solve only Eq. (22a). The eigenvalues λ^2 of Eqs. (22a) and (22b) must be either complex-conjugate pairs or real. We find them to be real and (almost all) negative, perturbed only slightly from the eigenvalues of $-L^2$. The eigenvalues λ of Eq. (17) are therefore found to be either pure imaginary or pure real, with most imaginary.

Problems (17), and (22a) and (22b) have neutral eigenmodes that reflect the physical invariances of the problem. Since $DW^I\Psi = W(\Psi)$, then the stationary state Ψ is a neutral mode of $L + DW^I$ and hence of problem (22b). This neutral mode is the phase mode of Eq. (6), since its existence is a consequence of the invariance of solutions Ψ to Eq. (12) under multiplication by any complex number on the unit circle. The corresponding eigenmode of problem (22a) is $d\Psi/d\mu$. This neutral mode can be understood as a consequence of differentiating (6) with respect to μ,

$$0 = \frac{d}{d\mu}[(L + W)\Psi] = (L + DW^R)\frac{d\Psi}{d\mu} + \Psi. \tag{23}$$

Thus,

$$-(L + DW^I)(L + DW^R)\frac{d\Psi}{d\mu} = (L + DW^I)\Psi = 0. \tag{24}$$

In terms of the original problem (17), the phase mode $(\lambda, \psi^R, \psi^I) = (0, 0, \Psi)$ is a neutral eigenvector, while Eq. (23)

shows that $(\lambda,\psi^R,\psi^I)=(0,d\Psi/d\mu,0)$ is a neutral generalized eigenvector, the two modes forming a Jordan block for Eq. (17).

In practice, we fix μ to calculate the stationary states Ψ and the eigenvalues. The operators of Eqs. (22a) and (22b) depend on μ both explicitly and through Ψ. For μ above a critical value μ_c, all eigenvalues λ are imaginary, i.e., Ψ is an elliptic stationary state of Eq. (9). As μ crosses μ_c, we will see that one imaginary pair fuses at zero, and becomes real, with one positive and one negative value of λ for $\mu<\mu_c$. Stationary states for $\mu<\mu_c$ are thus hyperbolic in the directions corresponding to these eigenvalues.

III. BIFURCATION AND STABILITY OF CONDENSATES

In this section, we will find the stationary solutions and study the stability of isotropic ($\omega_r=\omega_z$), cigarlike ($\omega_r/5=\omega_z$), and pancakelike ($\omega_r=\omega_z/5$) condensates. These results were obtained by solving Eq. (12) for the stationary states and Eq. (17) or Eq. (22a) for the corresponding bifurcating eigenvalues. The system is discretized using pseudospectral methods in a spherical domain for the isotropic case and in a periodic Cartesian domain for the nonisotropic cases. We use Newton's method to calculate the branches of stationary states. The bifurcating eigenvalue is found in the isotropic case by diagonalizing the matrix corresponding to Eq. (17). In the nonisotropic case, we use instead the iterative inverse Arnoldi method, which requires only actions of the operator in Eq. (22a). The BICGSTAB variant of the conjugate gradient method is used to solve the linear systems required by both Newton's method and the inverse Arnoldi method. The numerical methods we use are described in greater detail in the Appendix.

A. Isotropic condensate

In order to compare our results with the existing experiments on quasi-isotropic condensates, we will use the following physical constants, corresponding to ^{7}Li atoms in a radial trap: $m=1.16\times10^{-26}$ kg, $\tilde{a}=-27.3a_0$ (with a_0 the Bohr radius), and $\hat{\omega}=(\tilde{\omega}_x\tilde{\omega}_y\tilde{\omega}_z)^{1/3}=908.41\mathrm{s}^{-1}$. These values yield $a=-5.74\times10^{-3}$. With these parameters, the mean-field approximation (6) is expected to be very reliable. Note that we ignore the contributions of noncondensed atoms. They interact with the condensate only through a nearly constant background density term, inducing no significant change in the dynamics of the system [22].

The values of the energy functional $\mathcal{E}$ and the (smallest absolute value) square eigenvalue λ^2 versus particle number $\mathcal{N}$ are shown as solid lines in Fig. 2 (top and bottom, respectively). The eigenvalues are imaginary on the metastable elliptic lower branch ($\lambda^2<0$) and real on the unstable hyperbolic upper branch ($\lambda^2>0$). Using Eq. (2) on stationary solutions, we obtain $d\mathcal{E}/d\mathcal{N}=\mu$. Thus, μ is the slope of $\mathcal{E}$ and the lower branches $\mathcal{E}_-$, λ_-^2 (respectively, upper branches $\mathcal{E}_+$, λ_+^2) are scanned for $\mu>\mu_c$ (respectively, $\mu<\mu_c$). The point $\mu=\mu_c$ determines the maximum number of particles $\mathcal{N}=\mathcal{N}_c$ for which stationary solutions exist. We have checked that all the other pairs of eigenvalues are imaginary on both branches (data not shown).

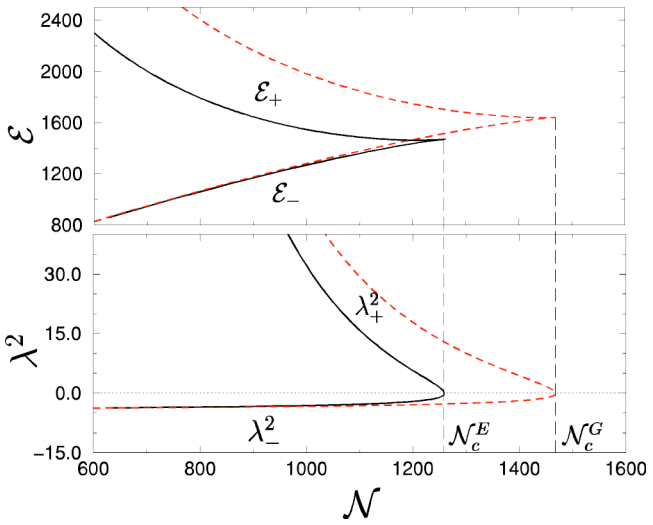

FIG. 2. Stationary solutions of the GP equation versus the particle number $\mathcal{N}$ for the isotropic potential case with $\hat{\omega}_r=\hat{\omega}_z=\hat{\omega}$. Top: value of the energy functional $\mathcal{E}_+$ on the unstable (hyperbolic) branch and $\mathcal{E}_-$ on the stable (elliptic) branch. Bottom: square of the bifurcating eigenvalue ($\lambda_\pm^2$). Note that $|\lambda_-|$ is the energy of small excitations around the stable branch. Solid lines: exact solution of the GP equation. Dashed lines: Gaussian approximation.

The dashed curves in Fig. 2 are derived from the Gaussian variational approximation that will be defined in Sec. III C for the general anisotropic case. In the present isotropic case, this approximation can be solved in closed form, yielding the expressions [15]

$$\mathcal{N}(\mu)=\frac{4\sqrt{2\pi^3}(-8\mu+3\sqrt{7+4\mu^2})}{7|\tilde{a}|(-2\mu+\sqrt{7+4\mu^2})^{3/2}}, \tag{25}$$

$$\mathcal{E}=\mathcal{N}(\mu)(-\mu+3\sqrt{7+4\mu^2})/7. \tag{26}$$

The number of particles $\mathcal{N}$ is maximal at $\mathcal{N}_c^G=8\sqrt{2\pi^3}/|5^{5/4}a|$ for $\mu=\mu_c^G=1/2\sqrt{5}$. The eigenvalues can also be obtained in closed form from the linearized equations of motion [15]:

$$\lambda^2(\mu)=8\mu^2-4\mu\sqrt{7+4\mu^2}+2. \tag{27}$$

By inspection of Fig. 2 it is apparent that both the solution of the GP equation and the Gaussian variational approximation share the same qualitative behavior, with quantitative discrepancies. Figure 3 shows the physical origin of the quantitative errors in the Gaussian approximation. It is apparent that the exact solution is well approximated by a Gaussian only for small $\mathcal{N}$ on the stable (elliptic) branch.

B. Hamiltonian saddle-node normal form

The qualitative behavior displayed in Fig. 2 by the physical quantities $\mathcal{E}$ and λ^2 near the critical value $\mathcal{N}=\mathcal{N}_c$ is the generic signature of a HSN bifurcation defined, at lowest order, by the normal form [23,24]

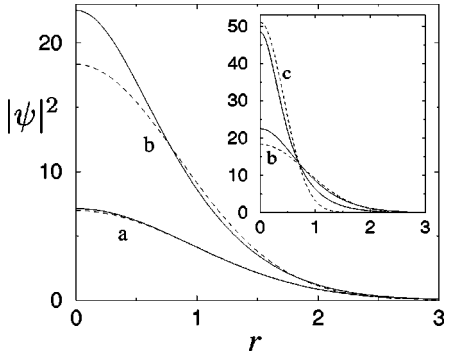

FIG. 3. Condensate density $|\psi|^2$ as a function of radius r, in reduced units (see text). Solid lines: exact solution of the GP equation. Dashed lines: Gaussian approximation. Stable (elliptic) solutions are shown for particle number $\mathcal{N}=252$ (a) and $\mathcal{N}=1132$ (b), and (c) is the unstable (hyperbolic) solution for $\mathcal{N}=1132$ (see inset).

$$\ddot{q}=\delta-\beta q^2, \tag{28}$$

where $\delta=(1-\mathcal{N}/\mathcal{N}_c)$ is the bifurcation parameter, β is a dimensionless constant, and q is the coordinate describing the state of the system in the direction of the phase space that becomes unstable. Indeed, introducing the additional nondimensional quantities $\mathcal{E}$ and γ to define the appropriate energy

$$\mathcal{E}=\mathcal{E}_0+\tfrac{1}{2}\dot{q}^2-\delta q+\tfrac{1}{3}\beta q^3-\gamma\delta, \tag{29}$$

it is straightforward to derive from Eq. (28) that, close to the critical point $\delta=0$, the universal scaling laws are given by

$$\mathcal{E}_{\pm}=\mathcal{E}_c-\mathcal{E}_l\delta\pm\mathcal{E}_\Delta\delta^{3/2}, \tag{30}$$

$$\lambda_{\pm}^2=\pm\lambda_\Delta^2\delta^{1/2}, \tag{31}$$

where $\mathcal{E}_c=\mathcal{E}_0$, $\mathcal{E}_l=\gamma$, $\mathcal{E}_\Delta=2/3\sqrt{\beta}$, and $\lambda_\Delta^2=2\sqrt{\beta}$. Note that these relations can be inverted to obtain the parameters in Eq. (28) from the critical data. For the Gaussian approximation, the critical amplitudes can be computed from Eqs. (25) and (26). One finds

$$\mathcal{E}_c=\frac{4\sqrt{2\pi^3}}{5^{3/4}|a|}, \tag{32}$$

$$\mathcal{E}_\Delta=\frac{64\sqrt{\pi^3}}{5^{9/4}|a|}, \tag{33}$$

$$\lambda_\Delta^2=4\sqrt{10}. \tag{34}$$

For the exact solutions, we obtain the critical amplitudes $\mathcal{E}_\Delta=1340$ and $\lambda_\Delta^2=14.68$ by performing fits on the numerical data. Comparing both results, we find that the Gaussian approximation captures the bifurcation qualitatively, but with quantitative errors of 17% for $\mathcal{N}_c$ [14], 24% for $\mathcal{E}_\Delta$, and 14% for λ_Δ^2 in the isotropic case [15].

The phase portrait of the normal form is shown in Fig. 4. When $\delta=(1-\mathcal{N}/\mathcal{N}_c)>0$, Eq. (28) admits two fixed points

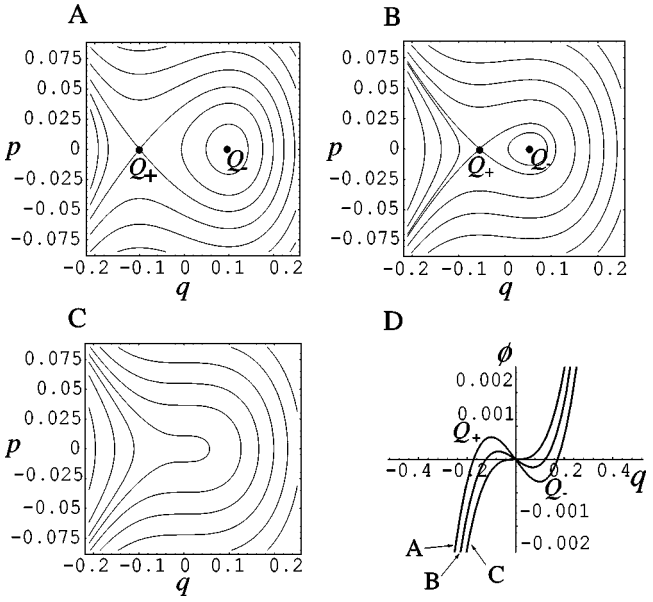

FIG. 4. Phase portraits of the Hamiltonian saddle-node normal form (28), with $p=\dot{q}$. (a) $\delta=0.2$, (b) $\delta=0.1$, (c) $\delta=0$. (d) Corresponding potential Φ associated with each phase portrait (a), (b), or (c), with $\dot{p}=-\partial\Phi/\partial q$. An elliptic region bounded by the separatrix that starts and ends on the fixed point Q_+ (homoclinic orbit) is present in (a) and (b). Phase portrait (c) displays the critical merging of fixed points Q_+ and Q_+, and the disappearance of the elliptic region.

$Q_\pm=\mp\sqrt{\delta/\beta}$, as shown in Fig. 4(a). Thus, a hyperbolic stationary state and an elliptic stationary state coexist. The phase space is separated into two regions by a separatrix that is a homoclinic orbit linking the hyperbolic stationary state to itself. Trajectories inside the orbit remain bounded near the elliptic fixed point. If the condensate is taken beyond the separatrix by a perturbation (e.g., thermal excitations or quantum tunneling, see Sec. IV below), it will fall into unbounded (hyperbolic) trajectories and collapse. As $\mathcal{N}$ is increased, the hyperbolic and elliptic stationary states approach one another, [Fig. 4(b)] and the homoclinic orbit inside which orbits are bounded is reduced. The two stationary states join at $\mathcal{N}=\mathcal{N}_c$ [Fig. 4(c)], at which the HSN occurs. No stationary state exists for $\mathcal{N}>\mathcal{N}_c$.

C. Nonisotropic condensates

We now briefly present the main expressions obtained from a Gaussian variational analysis of the GP equation with a cylindrical potential trap. Some of these results have been previously obtained by other authors [17,18,25–28]. We therefore restrict our discussion to the equations that will be used in our analysis of the condensate lifetimes.

The trial function is a Gaussian solution to the linear ($a=0$) Schrödinger equation in which we incorporate eight variational parameters in order to take into account the anisotropy of the system. The form of the ansatz is given by

$$\Psi(x,y,z,t)=[A_r(t)+iA_i(t)]\exp\left\{-\left(\frac{1}{X(t)^2}+i\phi_X(t)\right)\frac{x^2}{2}-\left(\frac{1}{Y(t)^2}+i\phi_Y(t)\right)\frac{y^2}{2}-\left(\frac{1}{Z(t)^2}+i\phi_Z(t)\right)\frac{z^2}{2}\right\}, \tag{35}$$

where the real parameters $\{A_r,A_i\}$, $\{\phi_X,\phi_Y,\phi_Z\}$, and $\{X,Y,Z\}$ are related to the amplitude, the phase and the width of the Gaussian profile, respectively. The Euler-Lagrange equations associated with the trial function (35) and the action defined in Eq. (1) can be reduced to the following system of second-order differential equations:

$$\frac{d^2X}{dt^2}=-\omega_x^2X-\frac{\nu}{X^2YZ}+\frac{1}{X^3},$$

$$\frac{d^2Y}{dt^2}=-\omega_y^2Y-\frac{\nu}{XY^2Z}+\frac{1}{Y^3},$$

$$\frac{d^2Z}{dt^2}=-\omega_z^2Z-\frac{\nu}{Z^2XY}+\frac{1}{Z^3}, \tag{36}$$

where

$$\nu=\sqrt{\frac{2}{\pi}}\frac{m(\omega_x\omega_y\omega_z)^{1/3}}{\hbar}|\tilde{a}|\mathcal{N}. \tag{37}$$

The evolution of the condensate is better understood by drawing an analogy between its width and the motion of a particle with coordinates (X,Y,Z) moving in the potential

$$U(X,Y,Z)=\frac{1}{2}(\omega_x^2X^2+\omega_y^2Y^2+\omega_z^2Z^2)-\frac{\nu}{XYZ}+\frac{1}{2}\left(\frac{1}{X^2}+\frac{1}{Y^2}+\frac{1}{Z^2}\right). \tag{38}$$

Indeed, defining $P_x=dX/dt$, $P_y=dY/dt$, $P_z=dZ/dt$, and the Hamiltonian

$$H(P_x,P_y,P_z,X,Y,Z)=\tfrac{1}{2}(P_x^2+P_y^2+P_z^2)+U(X,Y,Z),$$

we find that Eqs. (36) transform into Hamiltonian equations of motion.

If we consider now a potential trap (5) with cylindrical symmetry ($\omega_r\equiv\omega_x=\omega_y$) Eqs. (36) can be simplified by using $X(t)=Y(t)$. We thus find that Eq. (36) yields two fixed points (X_+,Z_+) and (X_-,Z_-), which describe the stationary solutions for $\Psi(x,y,z,t)$. These obey

$$0=\omega_r^2-\frac{4\mu}{7X_\pm^2}-\frac{5}{7X_\pm^4}+\frac{2}{7}\left(\frac{1}{X_\pm^2}+\frac{1}{Z_\pm^2}\right)\frac{1}{X_\pm^2}, \tag{39a}$$

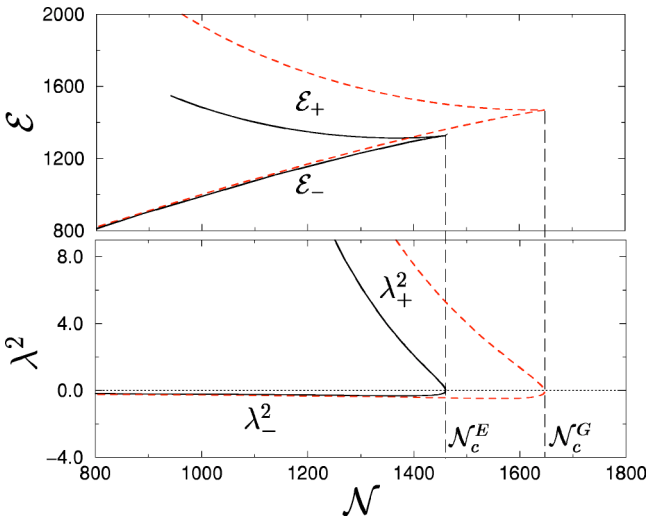

FIG. 5. Stationary solutions of the GP equation versus the particle number $\mathcal{N}$ for a nonisotropic potential case with $\omega_r=\hat{\omega}$ and $\omega_z=\hat{\omega}/5$ (cigar). Top: value of the energy functional. Bottom: square of the bifurcating eigenvalue ($\lambda_\pm^2$). Solid lines: exact solution of the GP equation. Dashed lines: Gaussian approximation.

$$0=\omega_z^2-\frac{4\mu}{7Z_\pm^2}-\frac{5}{7Z_\pm^4}+\frac{4}{7}\left(\frac{1}{X_\pm^2Z_\pm^2}\right), \tag{39b}$$

where the chemical potential μ is related to the total number of particles through

$$\mathcal{N}=\frac{2L_0}{7|\tilde{a}|}\sqrt{2\pi}X^2Z\left(\frac{1}{X^2}+\frac{1}{2Z^2}-\mu\right). \tag{40}$$

The fixed points correspond to a metastable center (X_+,Z_+) and to an unstable saddle point (X_-,Z_-), respectively. They are analogous to the Q_+ and Q_- points appearing in the phase portraits in Fig. 4. The solutions to Eq. (39) can be computed numerically, together with the linearized variational equations evaluated at every stationary point.

Figures 5 and 6 show $\mathcal{E}$ and λ^2 for the cigar and pancake cases, respectively. The solid lines present the values obtained by discretizing and solving numerically the original differential equations (12) and (22a), using the methods described in the Appendix. The dashed lines were computed using the Gaussian approximation described above. Both the isotropic and nonisotropic cases display saddle-node bifurcations. This is to be expected, since the saddle-node bifurcation is the generic way in which stable and unstable branches meet [23].

It is apparent from Figs. 2, 5, and 6 that the exact critical number of particles $\mathcal{N}_c^E$ is smaller than the Gaussian value $\mathcal{N}_c^G$ for all three geometries [8,14,17,18]. Table I compares the different critical $\mathcal{N}$ values obtained.

In order to compare properly the HSN bifurcations obtained for the three aspect ratios studied, we can rescale the intensity of the potential to obtain the same $\mathcal{N}_c^E$ for all cases. In general, any confining harmonic potential with frequen-

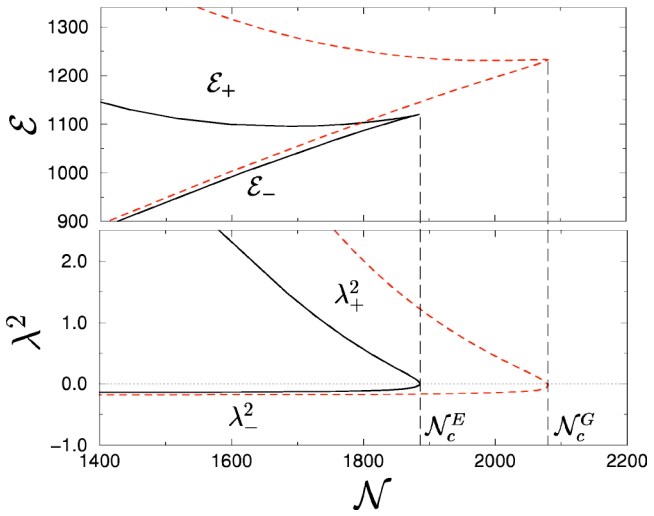

FIG. 6. Stationary solutions of the GP equation versus the particle number $\mathcal{N}$ for a nonisotropic potential case with $\omega_r=\hat{\omega}/5$ and $\omega_z=\hat{\omega}$ (pancake). Top: value of the energy functional. Bottom: square of the bifurcating eigenvalue ($\lambda_\pm^2$). Solid lines: exact solution of the GP equation. Dashed lines: Gaussian approximation.

cies ω_r and ω_z that produces a critical number of particles $\mathcal{N}_c$ can be rescaled by a factor

$$c=\left(\frac{\mathcal{N}_c}{\mathcal{N}_c^*}\right)^2, \tag{41}$$

to obtain a new potential with frequencies $\omega_r^*=c\,\omega_r$ and $\omega_z^*=c\,\omega_z$, which will have the critical number of particles $\mathcal{N}_c^*$. The remaining physical quantities for the new potential are obtained through the following transformations:

$$\Psi^*=\frac{\Psi}{c^{1/4}}, \tag{42}$$

$$\mathcal{N}^*=\frac{\mathcal{N}}{\sqrt{c}}, \tag{43}$$

$$\mathcal{E}^*=\frac{\mathcal{E}}{\sqrt{c}}, \tag{44}$$

$$\lambda^*=\lambda. \tag{45}$$

TABLE I. Critical number of particles obtained for the isotropic, cigar, and pancake geometries by using the exact solution of the GP equation ($\mathcal{N}_c^E$) and the Gaussian approximation ($\mathcal{N}_c^G$)

ω_r	ω_z	$\mathcal{N}_c^E$	$\mathcal{N}_c^G$
$\hat{\omega}$	$\hat{\omega}$	1258.5	1467.7
$\hat{\omega}$	$\hat{\omega}/5$	1460.3	1646.6
$\hat{\omega}/5$	$\hat{\omega}$	1885.6	2080.5

TABLE II. Rescaling factors required for having $\mathcal{N}_c=\mathcal{N}_c^{\rm iso}$ in the cigar and pancake cases. Columns $\mathcal{E}_\Delta$ and λ_Δ^2 show critical amplitudes at the bifurcation for the rescaled $\mathcal{E}$ and λ^2 curves, respectively.

ω_r	ω_z	Rescaling factor	$\mathcal{E}_\Delta$	λ_Δ^2
$\hat{\omega}$	$\hat{\omega}$		1340	14.68
$c_{\rm cig}\,\hat{\omega}$	$c_{\rm cig}\,\hat{\omega}/5$	$c_{\rm cig}=1.3463$	1000	4.00
$c_{\rm pan}\,\hat{\omega}/5$	$c_{\rm pan}\,\hat{\omega}$	$c_{\rm pan}=2.2447$	550	1.05

We choose arbitrarily to rescale the potential intensity so that all $\mathcal{N}_c^E$ are equal to that for the isotropic case $\mathcal{N}_c^{\rm iso}$. Table II shows the value of the rescaling factors $c_{\rm cig}$ and $c_{\rm pan}$ for the cigar and pancake cases, respectively, as obtained from Eq. (41) using $\mathcal{N}_c^*=\mathcal{N}_c^{\rm iso}$. The last two columns of this table show the critical amplitudes obtained for the rescaled $\mathcal{E}$ and λ^2 curves. These were obtained by fitting the HSN asymptotic forms given in relations (30) and (31) to the rescaled data.

IV. LIFETIME OF CONDENSATES

In this section, we first find expressions for the TIC, MQT, and ICO decay rates. Using the numerical data presented in the preceding section, we then compute these decay rates for the $\omega_r=\omega_z$ (isotropic), $\omega_r/5=\omega_z$ (cigar), and $\omega_r=\omega_z/5$ (pancake) cases. Finally, we compare the results obtained for these three potential geometries by studying the spontaneous isotropization of the condensates.

A. Definition and computations of decay rates

The TIC (thermally induced collapse) decay rate Γ_T is estimated using the formula [29]

$$\frac{\Gamma_T}{\hat{\omega}}=\frac{|\lambda_+|}{2\pi}\exp\left[\frac{-\hbar\hat{\omega}}{k_BT}(\mathcal{E}_+-\mathcal{E}_-)\right], \tag{46}$$

where $\hbar\hat{\omega}(\mathcal{E}_+-\mathcal{E}_-)$ is the (dimensionalized) height of the nucleation energy barrier (with $\hat{\omega}$ the reference frequency introduced in Sec. II A), T is the temperature of the condensate, and k_B is the Boltzmann constant. Note that the prefactor characterizes the typical decay time which is controlled by the slowest part of the nucleation dynamics: the top-of-the-barrier saddle-point eigenvalue λ_+ and not λ_- as used in Ref. [9]. However, near the bifurcation both eigenvalues scale in the same way and the behavior of Γ_T can be obtained directly from the universal saddle-node scaling laws (30) and (31). Thus, the exponential factor and the prefactor vanish, respectively, as $\delta^{3/2}$ and $\delta^{1/4}$.

We estimate the MQT (macroscopic quantum tunneling) decay rate using an instanton technique that takes into account the semiclassical trajectory giving the dominant contribution to the quantum action path integral [8,9]. We approximate this so-called bounce trajectory by the solution of the equation of motion

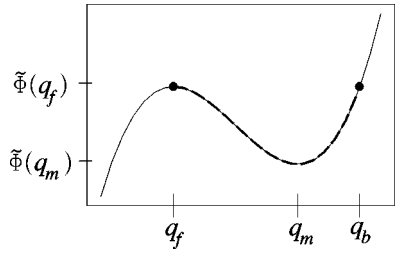

FIG. 7. Bounce trajectory (dashed) over the Euclidean potential $\tilde{\Phi}(q)$. Points q_f, q_m, and q_b indicate the fixed point, the minimum of $\tilde{\Phi}(q)$, and the bounce point, respectively.

$$\frac{d^2q(t)}{dt^2} = \frac{-d\tilde{\Phi}(q)}{dq}, \tag{47}$$

starting and ending at the fixed point q_f of the phase space where $\mathcal{E}(q_f)=\mathcal{E}_-$. The Euclidean potential $\tilde{\Phi}(q)$ is defined so that $-\tilde{\Phi}(q)$ reconstructs the Hamiltonian dynamics in the region scanned by the bounce trajectory (see Fig. 7). We represent it by a fourth-order polynomial of the form

$$\tilde{\Phi}(q)=\alpha_0+\alpha_2 q^2+\alpha_3 q^3+\alpha_4 q^4, \tag{48}$$

coefficients α_0, α_2, α_3, and α_4 chosen such that

$$\tilde{\Phi}(0)=-\mathcal{E}_+, \tag{49a}$$

$$\tilde{\Phi}(q_f)=-\mathcal{E}_-, \tag{49b}$$

$$\partial_q^2\tilde{\Phi}(0)=-\lambda_+(\mathcal{N}), \tag{49c}$$

$$\partial_q^2\tilde{\Phi}(q_f)=-\lambda_-(\mathcal{N}). \tag{49d}$$

We thus obtain a semianalytic polynomial expression for $\tilde{\Phi}(q)$ where the coefficients are determined through the numerical values presented in Figs. 2, 5, and 6.

Once $\tilde{\Phi}(q)$ and the bounce point q_b [defined through the relation $\tilde{\Phi}(q_b)=\tilde{\Phi}(q_f)$] are known, the MQT rate is estimated as

$$\frac{\Gamma_Q}{\hat{\omega}} = \sqrt{\frac{|\lambda_-|v_0^2}{4\pi}}\exp\left[\frac{-4}{\sqrt{2}}\int_{q_f}^{q_b}\sqrt{\tilde{\Phi}(q)-\tilde{\Phi}(q_f)}dq\right], \tag{50}$$

where v_0 is defined by the asymptotic form of the bounce trajectory $q(t)$ as it approaches q_f [9], given by $q(\tau)\sim q_f+(v_0/|\lambda_-|)\exp[-|\lambda_-|\tau]$.

In the same way as was done for the TIC, universal scaling laws can be derived close to criticality from Eq. (28), (30), and (31). We find that the exponential factor in Eq. (50) follows the same scaling as $\sqrt{|\mathcal{E}_+-\mathcal{E}_-|}dq$. It therefore vanishes as $\sqrt{\delta^{3/2}}\delta^{1/2}=\delta^{5/4}$. The asymptotic form of $q(t)$ shows that dq follows the same law as $v_0/|\lambda_-|$. Thus, $v_0\sim\delta^{3/4}$ and the prefactor vanishes as $\sqrt{\delta^{1/4}}\delta^{3/4}=\delta^{7/8}$. Note that these universal scaling laws agree with those already derived in the Gaussian case in Ref. [8].

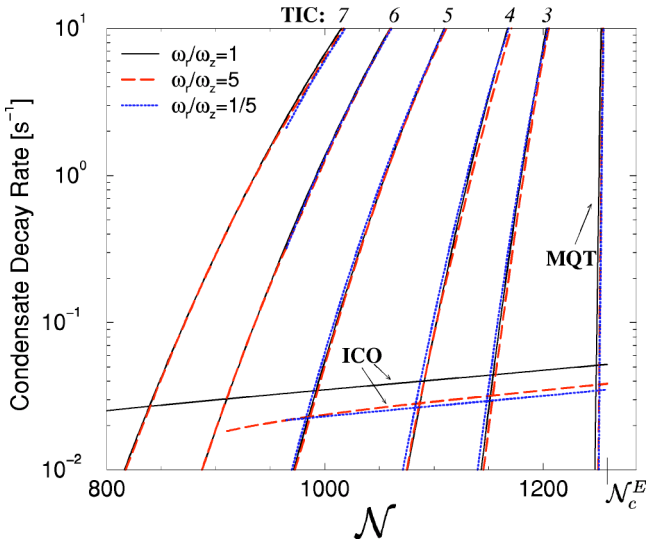

FIG. 8. Condensate decay rates versus particle number for the isotropic potential $\omega_r=\omega_z=\hat{\omega}$ (solid), and for the rescaled cigar potential $\omega_r=c_{\rm cig}\hat{\omega}$, $\omega_z=c_{\rm cig}\hat{\omega}/5$ (dashed), and pancake potential $\omega_r=c_{\rm pan}\hat{\omega}/5$, $\omega_z=c_{\rm pan}\hat{\omega}$ (dotted). ICO, inelastic collisions; MQT, macroscopic quantum tunneling; TIC, thermally induced collapse at temperatures 50 nK (3), 100 nK (4), 200 nK (5), 300 nK (6), and 400 nK (7).

The TIC (46) and MQT (50) decay rates obtained for the exact and Gaussian stationary states are shown in Fig. 8. To validate these results, we checked that the Gaussian TIC decay rates computed in Ref. [13] are found when we (incorrectly at a finite distance from criticality) replace λ_+ by λ_- in Eq. (46) (data not shown). We also checked that our Gaussian MQT decay rate agrees with the one previously computed in Ref. [8].

The ICO (inelastic two- and three-body collision) atomic decay rates are evaluated using the formula $d\mathcal{N}/dt=f_C(\mathcal{N})$ with

$$f_C(\mathcal{N})=K\int|\Psi|^4\,d^3\mathbf{x}+L\int|\Psi|^6\,d^3\mathbf{x}, \tag{51}$$

where $K=3.8\times10^{-4}$ s^{-1} and $L=2.6\times10^{-7}$ s^{-1} as in Refs. [10,11]. In order to compare the particle decay rate (51) to the condensate collective decay rates obtained for the TIC and MQT, we compute the condensate ICO half-life using

$$\tau_{1/2}(\mathcal{N})=\int_{\mathcal{N}/2}^{\mathcal{N}}\frac{dn}{f_C(n)}, \tag{52}$$

and plot $\tau_{1/2}^{-1}$ in Fig. 8.

Figures 8 and 9 compare the condensate decay rates for the isotropic and the cigar and pancake potentials, rescaled by $c_{\rm cig}$ and $c_{\rm pan}$ as described in Sec. III C. We note that the three aspect ratios generate very similar results after rescaling. The relative magnitudes of the different decay rates—TIC, MQT, and ICO—are the same for the three cases. At $T\leqslant1$ nK, the MQT effect becomes important compared to the ICO decay in a region very close to $\mathcal{N}_c^E$ ($\delta\leqslant8\times10^{-3}$). This was shown in Ref. [8] using Gaussian

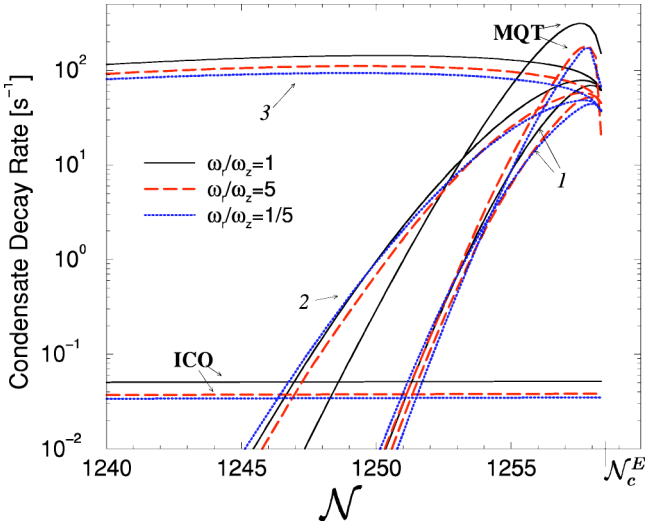

FIG. 9. Enlargement of the crossover region between the quantum tunneling and the thermal decay rate. ICO, inelastic collisions; MQT, macroscopic quantum tunneling; TIC, thermally induced collapse at temperatures 1 nK (1), 2 nK (2), and 50 nK (3).

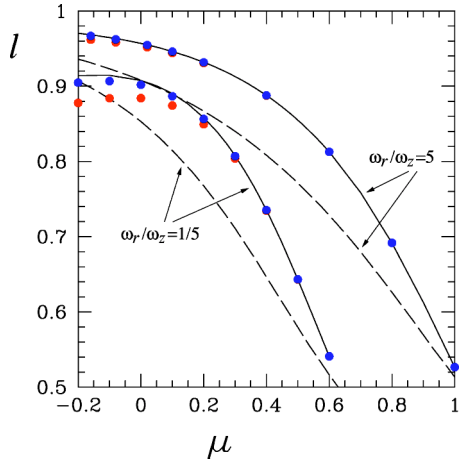

FIG. 10. Ellipticity ratio ℓ as a function of μ. Solid curves show numerical results and dashed curves the Gaussian approximation. For the cigar, $\ell \equiv \ell_r/\ell_z$ (upper curves) and for the pancake, $\ell \equiv \ell_z/\ell_r$ (lower curves). Dots show results obtained by using successively fewer Fourier modes in the numerical results; dots nearer to (further from) each curve correspond to retaining 7/8 (6/8) of the Fourier modes. ℓ changes by less than 1% for $\mu > -0.8$ ($\mu > -0.2$) for the cigar (pancake) case and by less than 0.1% at the saddle-node bifurcation at $\mu = 0.38$ ($\mu = 0.31$) for the cigar (pancake) case.

computations but evaluating them with the exact maximal number of condensed particles $\mathcal{N}_c^E$. Figure 9 shows that even for temperatures as low as 2 nK, the TIC decay rate exceeds the MQT rate except in a region extremely close to $\mathcal{N}_c$ ($\delta < 5 \times 10^{-3}$), where the condensates will live less than 10^{-1} s. Thus, in the experimental case of ^{7}Li atoms, the relevant effects are ICO and TIC, with the crossover that is shown in Fig. 9.

B. Spontaneous isotropization of condensates

The decay rates of the isotropic and nonisotropic cases shown in Fig. 8 are quite similar, despite the fact that ω_z and ω_r differ by a factor of 5. We have investigated this question by examining the wave functions Ψ for the pancake and cigar cases. These wave functions are peaked at the origin, as shown in Fig. 3. Their characteristic length scales in the axial and radial directions, ℓ_z and ℓ_r, can be measured by computing the ratios of the value of Ψ to its curvature at the origin.

More specifically, we define

$$\ell_z^2 \equiv \Psi \left(\frac{\partial^2 \Psi}{\partial z^2} \right)^{-1} \quad (r=0,\ z=0), \tag{53a}$$

$$\ell_r^2 \equiv \Psi \left(\frac{1}{r} \frac{\partial}{\partial r} r \frac{\partial \Psi}{\partial r} \right)^{-1} \quad (r=0,\ z=0). \tag{53b}$$

We then obtain the ellipticity of the wave function as the ratio ℓ of these length scales: $\ell = \ell_r/\ell_z$ for the cigar and $\ell = \ell_z/\ell_r$ for the pancake. These ellipticity ratios are shown in Fig. 10 as a function of μ. For large μ, i.e., away from the saddle-node bifurcation along the stable branch, ℓ decreases rapidly away from one, indicating that the wave function is highly nonisotropic. At the saddle-node bifurcation, $\ell = 0.89$ at $\mu = 0.38$ for the cigar and $\ell = 0.80$ at $\mu = 0.31$ for the pancake. As μ is decreased, i.e., as we leave the saddle-node bifurcation along the unstable branch, ℓ approaches 1 as the wave function becomes more spherically symmetric. This trend is present both in the numerical solution to the GP equation and in the Gaussian approximation, as can be seen in Fig. 10. Since the decay rates result from the scaling behavior near the saddle-node bifurcation, where the condensate is fairly isotropic, it follows that the decay rates are similar for the cigar, pancake, and spherically symmetric geometries, as we have shown in Figs. 8 and 9.

The spontaneous isotropization of condensates when μ is decreased can be understood by the following phenomenological reasoning. When $-\mu$ grows, the balance of terms on the right-hand side of Eq. (6) changes. For small $-\mu$, it is dominated by the isotropic ∇^2 and the anisotropic $V(x)$ terms. But for large $-\mu$, the wave function Ψ is strongly peaked and the ∇^2 and nonlinear terms, both isotropic, become dominant.

Figure 10 also provides a test of our numerical spatial resolution. By computing the ellipticity ℓ for different Fourier truncation levels, we show that ℓ changes with the resolution for low μ, especially for the pancake case, where we used fewer Fourier modes than in the other calculations. Note, however, that our decay rate calculations only use results near the saddle-node bifurcation, where ℓ varies by less than 0.1% when different truncation levels are used. This indicates that Ψ was adequately resolved in the region of interest.

As μ is decreased, the wave functions become more highly peaked for both our numerical results and for the Gaussian approximation (see Figs. 3 and 11). This is the main reason for the declining accuracy. To continue the com-

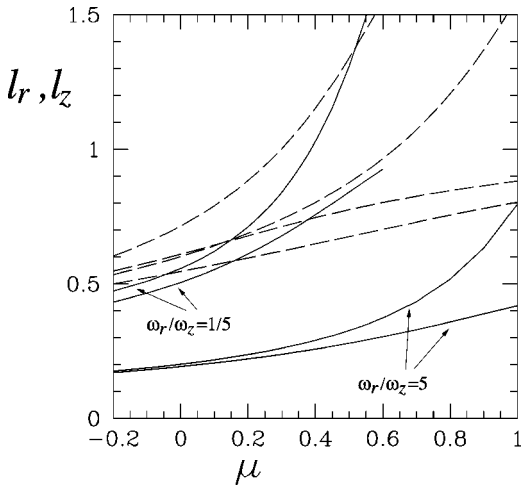

FIG. 11. Length scales ℓ_r, ℓ_z as a function of μ. Solid curves show numerical results and dashed curves the Gaussian approximation. The cigar case is shown in lower curves (with $\ell_r < \ell_z$) and the pancake in upper curves (with $\ell_z < \ell_r$). The size of the condensate decreases drastically as μ decreases, i.e., away from the saddle-node bifurcation along the unstable branch.

putations further, the size of the periodic box should be reduced along with μ. We believe that, with adequate resolution, all of the exact wave functions would become spherically symmetric as μ decreases, as do the Gaussian approximations.

V. CONCLUSION

We have demonstrated that it is possible to numerically compute the stationary states, the bifurcating eigenvalues, and the lifetime of anisotropic attractive Bose-Einstein condensates.

The Gaussian mean-field approximation was found to have significant quantitative errors for all the different confining potential geometries that were studied, when compared with numerical solutions to the GP equation.

Spontaneous isotropization of the metastable condensate was found to occur as the critical number of particles is approached, yielding a lifetime that depends weakly on the anisotropy of the confining potential.

Direct methods—Gaussian elimination and diagonalization—were used in treating the spherically symmetric case, of size 128, but are far too costly for the three-dimensional case, of size 10^6. In fact, since we only calculated axisymmetric stationary states and eigenvectors with an additional midplane symmetry, an intermediate two-dimensional axisymmetric cylindrical representation could have been implemented, of size 5000, permitting the use of direct methods. Our purpose, however, has been to construct and explore numerical methods appropriate for a general nonisotropic case.

The methods used to compute stationary states and bifurcating eigenvalues for the nonisotropic cases are essentially analogous. Each consists of a powerful and rapid outer iteration: Newton's method for the stationary states and the inverse Arnoldi method for the eigenvalues. The large linear systems that need to be inverted within each method are solved by the same inner biconjugate gradient iteration—BICGSTAB—and constitute the main numerical difficulty. Its convergence is greatly improved by an inverse Laplacian preconditioning which is empirically tuned by adjusting the pseudotime step σ in Newton's method or the shift s in Arnoldi's method.

Our results and implementation have demonstrated that all these numerical techniques can be successfully combined to calculate the stationary states and eigenvectors for the GP equation in a confining potential with an arbitrary three-dimensional geometry.

ACKNOWLEDGMENTS

This work was supported by ECOS-CONICYT Program No. C01E08 and by NSF Grant No. DMR-0094569. Computations were performed at the Institut du Développement et des Ressources en Informatique Scientifique (IDRIS) of the CNRS.

APPENDIX: NUMERICAL METHODS

1. Spatial discretization

The operators L and W defined in Eqs. (10) and (11) are spatially discretized using the pseudospectral method [30]. For the isotropic case, the spherically symmetric $\Psi(r,t)$ is expanded as a series of even Chebyshev polynomials $T_{2n}(r/R)$, on which the boundary condition $\Psi(R,t)=0$ is imposed. The domain is taken to be $0 \leqslant r \leqslant R=4$ and the resolution used is $N_R=128$. For the nonisotropic cases, we use a three-dimensional periodic Cartesian domain and Ψ is expanded as a three-dimensional trigonometric (Fourier) series. The cigar case is solved in a periodic domain of size $(L_x,L_y,L_z)=(5.39,5.39,12.04)$ in units of L_0, using $(N_x,N_y,N_z)=(96,96,96)$ grid points or trigonometric modes (with a 2/3 dealiasing rule), so the total number of grid points or trigonometric functions is as high as $N_{3D}=10^6$. [The more poorly resolved pancake case was calculated using $(L_x,L_y,L_z)=(12.04,12.04,5.39)$ and $(N_x,N_y,N_z)=(48,48,96)$.] The harmonic potential (5) is approximated by a periodic potential by writing $x=\arcsin[\sin(x)]$ and Taylor expanding the arcsin function. This leads to a Fourier series for the potential, which is truncated according to the resolution used.

Pseudospectral methods require performing over Ψ, at every iteration, a Chebyshev transform in the isotropic case or a Fourier transform in the nonisotropic case. These operations consume a time proportional to $N_R \ln N_R$ or $N_{3D}\ln(N_{3D})$, respectively. Actions and inversions of the Laplacian L are carried out on the Chebyshev or Fourier representations of Ψ, while actions of the multiplicative operator W are carried out on its grid representations. The time required by these operations scales approximately linearly in N_R or N_{3D}.

2. Stationary states

As stated in Sec. II B, the stationary states of Eq. (6) that correspond to minima of $\mathcal{E}$ at a given value of $\mathcal{N}$ can be obtained by integrating to relaxation the diffusion equation

$$\frac{\partial \Psi}{\partial t} = L\Psi + W(\Psi), \tag{A1}$$

where the initial data $\Psi(t=0)$ has a total number of particles $\mathcal{N}$ and the value of the Lagrange multiplier μ is fixed during the relaxation by the condition $\partial \mathcal{N}/\partial t = 0$.

To integrate Eq. (A1), a mixed implicit-explicit first-order time-stepping scheme is used:

$$\Psi(t+\sigma) = (I-\sigma L)^{-1}(I+\sigma W)\Psi(t), \tag{A2}$$

where I is the identity operator. The Helmholtz operator $(I-\sigma L)^{-1}$ is easily inverted in the Chebyshev or Fourier representation. The motivation for integrating L implicitly is to avoid the extremely small time steps that would otherwise be necessitated by the wide range of eigenvalues of the Laplacian.

This relaxation method is equivalent to that used in Ref. [14] and can only reach the stable stationary solutions of Eq. (A1). In order to also capture unstable stationary solutions [31], we implemented a Newton branch-following algorithm [15,32]. We search for fixed points of Eq. (A2), a condition strictly equivalent to the stationarity of Eq. (6):

$$\begin{aligned} 0 &= B\Psi(t) \equiv \Psi(t+\sigma) - \Psi(t) \\ &= (I-\sigma L)^{-1}(I+\sigma W)\Psi(t) - \Psi(t) \\ &= [(I-\sigma L)^{-1}(I+\sigma W) - I]\Psi(t) \\ &= (I-\sigma L)^{-1}[(I+\sigma W) - (I-\sigma L)]\Psi(t) \\ &= (I-\sigma L)^{-1}[(\sigma(L+W)]\Psi(t). \end{aligned} \tag{A3}$$

Solutions to Eq. (A3) are found using Newton's method. We begin with an initial estimate Ψ, in our case the solution at a neighboring value of μ. Newton's method calls for approximating the nonlinear operator B whose roots are sought by its linearization B_Ψ about Ψ. We seek a decrement ψ such that $\Psi - \psi$ solves this linearized equation

$$\begin{aligned} 0 = B(\Psi - \psi) &\approx B(\Psi) - B_\Psi \psi, \\ B_\Psi \psi &= B(\Psi). \end{aligned} \tag{A4}$$

Ψ is then replaced by $\Psi - \psi$ and Eq. (A4) is solved again for a further decrement. The process is iterated until $B(\Psi)$ or ψ is sufficiently small. In our case, Eq. (A4) takes the form

$$(I-\sigma L)^{-1}\sigma(L+DW)\psi = (I-\sigma L)^{-1}\sigma(L+W)\Psi. \tag{A5}$$

We will explain how we solve the large linear problem (A5) in the following section.

The role of σ is formally that of the time step in Eq. (A2), but in Eq. (A5), its value can be taken to be arbitrarily large. For $\sigma \to \infty$, Eq. (A5) becomes

$$L^{-1}(L+DW)\psi = L^{-1}(L+W)\Psi. \tag{A6}$$

For the spherically symmetric case, the linear system (A6) is of size $N_R = 128$ and can be solved by standard Gaussian elimination. The boundary condition $\psi(r=R)=0$ is imposed by modifying the operator L^{-1} or $(I-\sigma L)^{-1}$, as it is in the time-stepping algorithm (A2).

To compute the full branch of solutions as a function of μ, we begin from a stable state of Eq. (A1) at a small value of $\mathcal{N}$ obtained by time integration. Each stationary state is computed in three to five Newton iterations.

3. Conjugate gradient solution of linear systems

For the periodic Cartesian case, the linear system (A6) of size $N_{3D} = 10^6$ is too large to be stored or inverted directly: the operation count for Gaussian elimination would be of the order of N_{3D}^3. Instead, we use BICGSTAB [33], a variant of the well-known conjugate gradient method, developed for linear systems that are not symmetric definite. Such methods are matrix-free, meaning that they require only the right-hand-side of Eq. (A6), and a subroutine that acts with the linear operator of the left-hand side. A solution to the linear system is constructed as a carefully chosen linear combination of powers of the linear operator acting on the right-hand side.

For a periodic Cartesian geometry, conjugate gradient methods are particularly economical, since operator actions are all accomplished in a time proportional to N_{3D}. However, conjugate gradient methods for nonsymmetric definite systems may converge slowly (requiring a large number of evaluations of the linear operator) or even not at all. This happens when the operator is poorly conditioned, i.e., roughly when it has a wide range of eigenvalues. One must then precondition the linear system, i.e., multiply both sides of the system by a matrix which improves its conditioning and accelerates convergence. Since for operators such as $L+DW$, the wide range of eigenvalues is due primarily to those of L, we expect L^{-1} to be an effective preconditioner. From Eq. (A5), it can be seen that σ allows us to interpolate between linear operators $\sigma(L+DW)$ and $L^{-1}(L+DW)$. We vary σ empirically to optimize the convergence of BICGSTAB. A few hundred BICGSTAB iterations are usually required to solve the linear system.

A further advantage of iterative inversion methods is that they can produce a (nonunique) solution even when the linear operator is singular. This is the case for our operators, which have the neutral modes described in Sec. II C, as well as other neutral modes related to symmetries and the Fourier representation. The preconditioner, however, is inverted exactly. If Eq. (A6) is used, the constant Fourier mode is treated separately which allows us to construct an invertible version of the singular operator L.

4. Eigenvalue problem

We now describe our numerical method for calculating the linear stability of the stationary states. For the spherically symmetric case, the eigenvalues of Eq. (17) are computed by constructing and diagonalizing the corresponding matrix for each converged stationary solution. The results reported were

generated with a MATHEMATICA code running on a workstation. With the values $R=4$, $N_R=128$, the first two eigenvalues of the harmonic oscillator are obtained with a precision better than 0.05%.

For the three-dimensional case, it is again not possible to construct and diagonalize the matrix of size $N_{3D}=10^6$ directly: the operation count for diagonalization is also of the order of N_{3D}^3. Instead, we calculate only eigenvalues of interest, using a variant of the iterative inverse power method. The inverse power method calculates the eigenvalues of a matrix M closest to a value s by means of the sequence defined by

$$(M-sI)\psi_{j+1}=\psi_j . \tag{A7}$$

The sequence $\{\psi_j\}$ converges rapidly to the eigenvector whose eigenvalue is nearest to s, with the eigenvalue λ of M estimated by $(\lambda-s)^{-1}\approx\langle\psi_{j+1},\psi_j\rangle/\langle\psi_j,\psi_j\rangle$.

In order to calculate complex or multiple eigenvalues and to obtain more precise eigenvalues and error estimates, we use the sequence generated by Eq. (A7) to implement the more general Arnoldi or Krylov method [32,34]. Instead of retaining only the last two members of the sequence, the last K members (typically 4 or 6) are orthonormalized and then assembled into the $K\times K$ matrix $H_{jk}\equiv\langle\psi_j,(M-sI)^{-1}\psi_k\rangle$. The eigenvalues of H provide estimates of up to K of the eigenvalues $(\lambda-s)^{-1}$ of $(M-sI)^{-1}$.

In our implementation of the Arnoldi method for Eq. (22a), we seek the eigenvalues λ^2 of the matrix $-(L+DW^I)(L+DW^R)$. Rather than solving Eq. (A7), we solve the equivalent preconditioned problem [32]

$$L^{-2}[-(L+DW^I)(L+DW^R)-sI]\psi_{j+1}=L^{-2}\psi_j , \tag{A8}$$

by using BICGSTAB. From Eq. (A8), we obtain a sequence of vectors containing an increasing proportion of the desired eigenvectors, but since our solution of Eq. (A8) is not exact, we then construct H by multiplication rather than inversion via $H_{jk}\equiv\langle\psi_j,M\psi_k\rangle$. We can then estimate the eigenvalues λ^2 by those of H. Although the formal role of s is that of a shift which focuses the inverse iteration on the eigenvalues being sought, here we also use it empirically to improve the convergence of BICGSTAB.

The inverse Arnoldi method requires between three and ten iterations to converge, each of which requires several hundred BICGSTAB iterations in order to solve its associated linear system.

[1] C.C. Bradley, C.A. Sackett, J.J. Tollett, and R.G. Hulet, Phys. Rev. Lett. **75**, 1687 (1995).

[2] C.C. Bradley, C.A. Sackett, and R.G. Hulet, Phys. Rev. Lett. **78**, 985 (1997).

[3] J.L. Roberts, N.R. Claussen, S.L. Cornish, E.A. Donley, E.A. Cornell, and C.E. Wieman, Phys. Rev. Lett. **86**, 4211 (2001).

[4] K. Strecker, G. Partridge, A. Truscott, and R. Hulet, Nature (London) **417**, 150 (2002).

[5] F. Schreck, L. Khaykovich, K.L. Corwin, G. Ferrari, T. Bourdel, J. Cubizolles, and C. Salomon, Phys. Rev. Lett. **87**, 080403 (2001).

[6] F. Schreck, G. Ferrari, K.L. Corwin, J. Cubizolles, L. Khaykovich, M.-O. Mewes, and C. Salomon, Phys. Rev. A **64**, 011402 (2001).

[7] A. Görlitz, J.M. Vogels, A.E. Leanhardt, C. Raman, T.L. Gustavson, J.R. Abo-Shaeer, A.P. Chikkatur, S. Gupta, S. Inouye, T. Rosenband, and W. Ketterle, Phys. Rev. Lett. **87**, 130402 (2001).

[8] M. Ueda and A.J. Leggett, Phys. Rev. Lett. **80**, 1576 (1998).

[9] H.T.C. Stoof, J. Stat. Phys. **87**, 1353 (1997).

[10] H. Shi and W.-M. Zheng, Phys. Rev. A **55**, 2930 (1997).

[11] R.J. Dodd, M. Edwards, C.J. Williams, C.W. Clark, M.J. Holland, P.A. Ruprecht, and K. Burnett, Phys. Rev. A **54**, 661 (1996).

[12] Y. Kagan, G.V. Shlyapnikov, and J.T.M. Walraven, Phys. Rev. Lett. **76**, 2670 (1996).

[13] C.A. Sackett, H.T.C. Stoof, and R.G. Hulet, Phys. Rev. Lett. **80**, 2031 (1998).

[14] P.A. Ruprecht, M.J. Holland, K. Burnett, and M. Edwards, Phys. Rev. A **51**, 4704 (1995).

[15] C. Huepe, S. Métens, G. Dewel, P. Borckmans, and M.E. Brachet, Phys. Rev. Lett. **82**, 1616 (1999).

[16] A. Gammal, T. Frederico, and L. Tomio, Phys. Rev. E **60**, 2421 (1999).

[17] A. Gammal, L. Tomio, and T. Frederico, Phys. Rev. A **66**, 043619 (2002).

[18] A. Gammal, T. Frederico, and L. Tomio, Phys. Rev. A **64**, 055602 (2001).

[19] E.P. Gross, Nuovo Cimento **20**, 454 (1961).

[20] L.P. Pitaevskii, Zh. Eksp. Teor. Fiz. **40**, 646 (1961) [Sov. Phys. JETP **13**, 451 (1961)].

[21] Wen-Chin Wu and A. Griffin, Phys. Rev. A **54**, 4204 (1996).

[22] M. Houbiers and H.T.C. Stoof, Phys. Rev. A **54**, 5055 (1996).

[23] J. Guckenheimer and P. Holmes, *Nonlinear Oscillations, Dynamical Systems and Bifurcations of Vector Fields* (Springer-Verlag, Berlin, 1983).

[24] C. Elphick, E. Tirapegui, M.E. Brachet, P. Coullet, and G. Iooss, Physica D **29**, 95 (1987).

[25] V.M. Pérez-Garcia, H. Michinel, J.I. Cirac, M. Lewenstein, and P. Zoller, Phys. Rev. A **56**, 1424 (1997).

[26] V.M. Pérez-Garcia, H. Michinel, and H. Herrero, Phys. Rev. A **57**, 3837 (1998).

[27] F.K. Abdullaev, A. Gammel, L. Tomio, and T. Frederico, Phys. Rev. A **63**, 043604 (2001).

[28] S.K. Adhikari, Phys. Rev. E **65**, 016703 (2002).

[29] C. Gardiner, *Handbook of Stochastic Methods* (Springer-Verlag, Berlin, 1985).

[30] D. Gottlieb and S.A. Orszag, *Numerical Analysis of Spectral Methods* (SIAM, Philadelphia, 1977).

[31] R. Seydel, *From Equilibrium to Chaos: Practical Bifurcation and Stability Analysis* (Elsevier, New York, 1988).

[32] L.S. Tuckerman and D. Barkley, in *Numerical Methods for Bifurcation Problems and Large-Scale Dynamical Systems*, edited by E. Doedel and L.S. Tuckerman, IMA Volumes in Mathematics and its Applications Vol. 119 (Springer, New York, 2000), pp. 452–466.

[33] H. van der Vorst, SIAM (Soc. Ind. Appl. Math.) J. Sci. Stat. Comput. **13**, 631 (1992).

[34] W.E. Arnoldi, Q. Appl. Math. **9**, 17 (1951).